ACSNANO
www.acsnano.org
ARTICLE

Ultrasmall Biocompatible Bi_2Se_3 Nanodots for Multimodal Imaging-Guided Synergistic Radiophototherapy against Cancer

Fangxin Mao,[†,‡] Ling Wen,[†] Caixia Sun,[†] Shaohua Zhang,[†] Guanglin Wang,[†] Jianfeng Zeng,[†] Yong Wang,[†] Jianmin Ma,[*,‡] Mingyuan Gao,[†] and Zhen Li[*,†]

[†]Center for Molecular Imaging and Nuclear Medicine, School for Radiological and Interdisciplinary Sciences (RAD-X), Soochow University, Collaborative Innovation Center of Radiation Medicine of Jiangsu Higher Education Institutions, Suzhou 215123, P. R. China

[‡]School of Physics and Electronics, Hunan University, Changsha 410082, P. R. China

Supporting Information

ABSTRACT: **Sub-3 nm ultrasmall Bi_2Se_3 nanodots stabilized with bovine serum albumin were successfully synthesized through a reaction of hydroxyethylthioselenide with bismuth chloride in aqueous solution under ambient conditions. These nanodots exhibit a high photothermal conversion efficiency (η = 50.7%) due to their strong broad absorbance in the near-infrared (NIR) window and serve as a nanotheranostic agent for photoacoustic imaging and photothermal cancer therapy. In addition, they also display radioenhancement with a ratio of 6% due to their sensitivity to X-rays, which makes them a potential sensitizer for radiotherapy. These nanodots were also labled with radioactive ^{99m}Tc for quantification of their biodistribution by single-photon-emission computed tomography (SPECT)/computed tomography (CT) imaging. Our work demonstrates the potential of ultrasmall Bi_2Se_3 nanodots in multimodal imaging-guided synergetic radiophototherapy of cancer.**

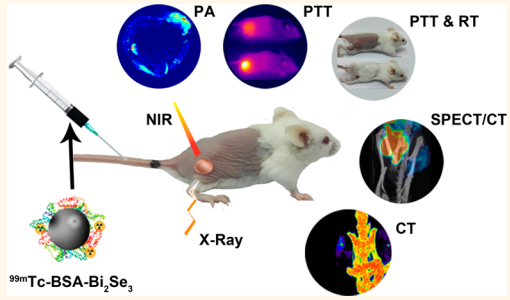

KEYWORDS: *multimodal imaging, radiophototherapy, bismuth selenide nanodots, ultrasmall, bovine serum albumin*

Despite the great efforts devoted to the fight against cancer over the past decades, precise detection and treatment of cancer at an early stage remains a big challenge.[1] Most tumors are not detected and treated until they grow to a large size, increasing the risk of metastasis and poor outcomes, due to the low sensitivity and specificity of currently available approaches. An alternative option is the combined use of complementary diagnostic and therapeutic methods that can overcome the shortcomings of individual approach. One example is the simultaneous use of multimodal imaging technologies, such as magnetic resonance imaging (MRI) and positron emission tomography (PET) for detection, and the combined use of surgery, radiotherapy (RT), and chemotherapy during treatment.[2−5] The simultaneous use of multimodal imaging and multiple therapies needs widely applicable nanotheranostic agents. In this context, nanoscale bismuth chalcogenides (Bi_2E_3, E = S, Se, and Te) agents, especially Bi_2S_3 and Bi_2Se_3, have attracted considerable attention due to the biosafety of bismuth (*e.g.*, bismuth-containing compounds are widely used for treating peptic ulcer,[6] *Helicobacter pylori*,[7,8] and gastric diseases[9]) and their diverse applications, such as X-ray computed tomography (CT) imaging,[10] photoacoustic (PA) imaging,[11] photothermal therapy (PTT),[12] and radiotherapy.[13] For example, Bi_2S_3 nanoparticles embedded in mesoporous silica were proven to be an efficient radiosensitizer for inhibiting the growth of tumors during radiotherapy.[14] Sub-10 nm Bi_2S_3 nanoparticles coated with albumin demonstrated an enhanced contrast effect and radiosensitivity.[15] In addition, two-dimensional (2D) MoS_2/Bi_2S_3 nanocomposites also showed potential in CT imaging and enhanced radiotherapy for cancer.[16]

Compared with orthorhombic Bi_2S_3, Bi_2Se_3 has a layered rhombohedral structure and easily forms 2D nanocarriers, which have great potential for the imaging and treatment of cancer. For example, Bi_2Se_3 nanosheets show lower toxicity and better CT performance than iopamidol.[17] Recently, ultrathin Bi_2Se_3 nanosheets with a diameter of 31.4 nm and a thickness of 1.7 nm were proven to be an effective photoacoustic imaging agent due to their large extinction coefficient.[18] In addition to pure Bi_2Se_3 nanosheets, core−shell MnSe@Bi_2Se_3, $FeSe_2$-decorated Bi_2Se_3 nanosheets, and perfluorocarbon-loaded hollow Bi_2Se_3 nanoparticles were successfully employed for

Received: September 8, 2016
Accepted: November 16, 2016
Published: November 16, 2016

DOI: 10.1021/acsnano.6b06067
ACS Nano 2016, 10, 11145−11155

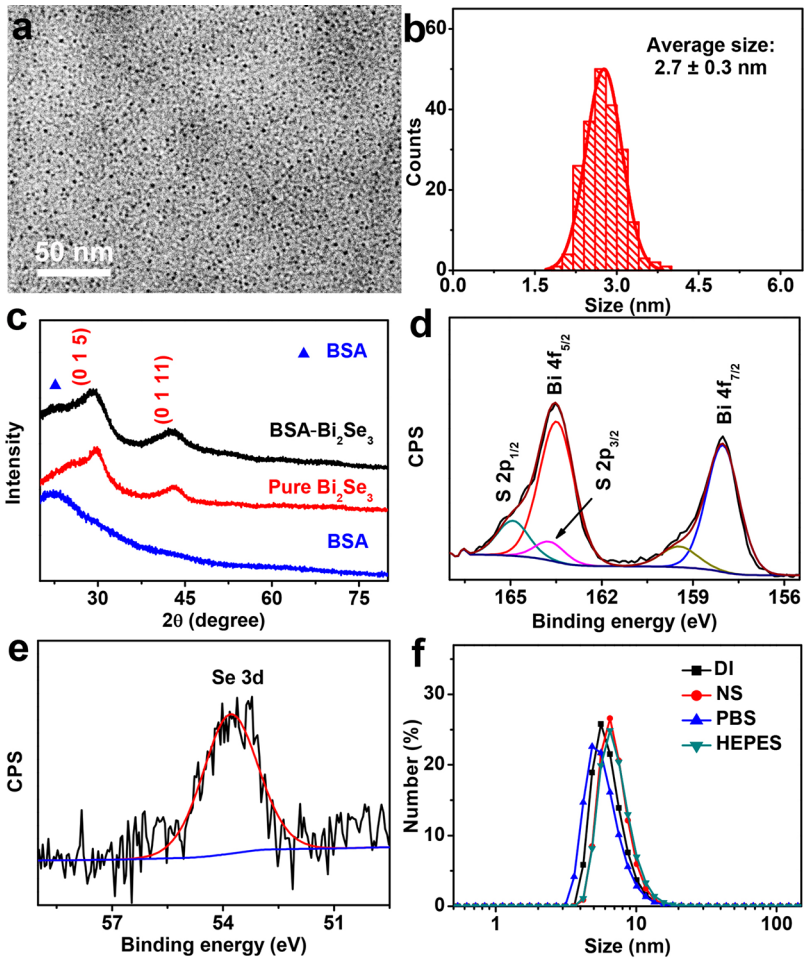

Figure 1. (a,b) TEM image and the size distribution of as-prepared BSA-Bi_2Se_3 nanodots. (c) XRD patterns of BSA-Bi_2Se_3 nanodots (black), pure Bi_2Se_3 (red), and pure BSA (blue), respectively. (d,e) XPS spectra of Bi_{4f} and Se_{3d} from BSA-Bi_2Se_3 nanopowder. (f) Hydrodynamic size of BSA-Bi_2Se_3 nanodots dispersed in different media including deionized water (DI), 0.9% NaCl solution (NS), neutral phosphate buffer solution (PBS), and piperazineethanesulfonic acid (HEPES).

MRI imaging, CT imaging, and radiothermotherapy for cancer.[19−21]

The above examples clearly illustrate the huge potential of Bi_2S_3 and Bi_2Se_3 nanostructures in multimodal imaging-guided therapy against cancers. Their application in CT imaging is mainly attributed to the high atomic number (Z = 83) and the large X-ray attenuation coefficient (*e.g.*, 5.74 cm^2 g^{-1} at 100 keV) of bismuth.[7] Their advantage in radiotherapy is due to the efficient emissions of Compton electrons, scattered photons, photoelectrons, electron-positron pairs, and Auger electrons upon high-energy irradiation.[22] Their applications in PA imaging and PTT are attributed to their high photothermal conversion efficiency arising from their narrow band gap and strong broad near-infrared absorbance.

Compared with nanoscale Bi_2S_3, Bi_2Se_3 nanostructures can release vital selenium for reducing the occurrence and fatality of liver, prostate, and lung cancers.[23] Nevertheless, well-defined monodisperse Bi_2Se_3 nanostructures are usually prepared in hydrophobic organic solvents due to the fast hydrolysis of Bi^{3+}, and laborious surface postmodification is needed to make them water-soluble and biocompatible for bioapplications. In addition, the resultant nanostructures have a large size, which increases their risks of rapid clearance by phagocytes and the reticuloendothelial system (RES) and reduces their accumulation in lesion tissue. The large size could also lead to their long metabolism and increase the risks of potential side effects.[24,25] In this context, direct preparation of a water-soluble and biocompatible ultrasmall Bi_2Se_3 nanotheranostic agent in aqueous solution under ambient conditions is highly significant.

Preparation of Bi_2Se_3 nanostructures in aqueous solution is usually carried out by reaction of Bi^{3+} ions with Se^{2-} ions. Water-soluble bismuth salts are commonly dissolved in an acidic solution to prevent the hydrolysis of Bi^{3+} ions, and Se powder is usually chosen as the Se^{2-} precursor and reduced by $NaBH_4$. It is difficult to control the stoichiometric ratio for completely reducing of Se powder, because both Se^{2-} and Se are easy to oxidize, and $NaBH_4$ could partially lose reactivity due to its sensitivity to moisture. These facts lead to difficulty in tuning Bi_2Se_3 nanostructures. Recently, we demonstrated that Se powder could be easily dissolved in mercaptoethanol in the presence of traces of base. The thiol group (−SH, logarithmic acid dissociation constant, pK_a = 9.61) in mercaptoethanol was deprotonated under the catalysis of the base to form chalcophilic hydroxyethylmercaptide, which could react with Se powder to produce highly reactive hydroxyethylthioselenide that further reacts with metal and metal ions to form various metal selenides nanostructures.[26−30]

In this article, ultrasmall biocompatible Bi_2Se_3 nanoparticles (2.7 ± 0.3 nm) were synthesized by the reaction of hydroxyethylthioselenide with bismuth chloride in aqueous

DOI: 10.1021/acsnano.6b06067
ACS Nano 2016, 10, 11145−11155

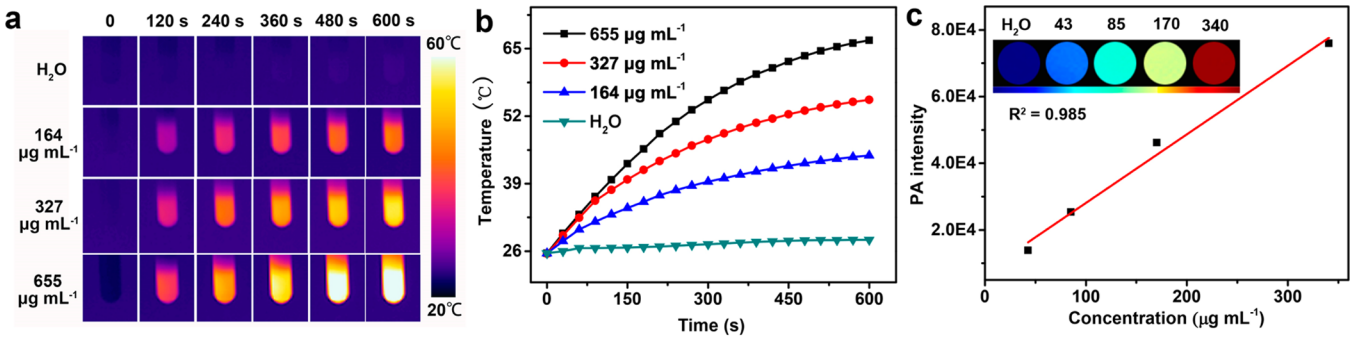

Figure 2. (a) Photos and (b) temperature variation of ultrasmall BSA-Bi_2Se_3 nanodots solutions with different concentrations (*i.e.*, 0, 164, 327, and 655 μg mL^{-1}), under irradiation by an 808 nm laser with a power density of 0.75 W cm^{-2} for 600 s. (c) Photoacoustic intensity linearly fit to the concentration of BSA-Bi_2Se_3 aqueous solutions; inset: the corresponding PA images.

solution in the presence of bovine serum albumin (BSA). The obtained ultrasmall nanodots (referred as BSA-Bi_2Se_3) exhibit strong broad absorbance in the near-infrared (NIR) window, high photothermal conversion efficiency, and a large radiosensitization. These nanodots were employed as nanotheranostic agents for trimodal imaging [PA/single-photon-emission computed tomography (SPECT)/CT] guided synergistic therapy (PTT/RT) for cancer.

RESULTS AND DISCUSSION

Figure 1a shows a transmission electron microscopy (TEM) image of as-synthesized ultrasmall BSA-Bi_2Se_3 nanodots. An ultrasmall size of 2.7 ± 0.3 nm is obtained from the statistical histogram in Figure 1b, which is much smaller than that of nanoparticles (12.2 ± 2.8 nm) prepared without BSA (Figure S1a,b in the Supporting Information). The formation of such small uniform nanoparticles is attributed to the extremely low solubility of Bi_2Se_3 (solubility constant, $K_{sp} = 10^{-130}$), the strong coordination of functional groups with Bi^{3+}, and the stearic hindrance effect of BSA. Their formation Gibbs free energy can be calculated by eqs 1 and 2), in which R is a constant, T is the temperature, K_{sp} is the solubility of product constant, and C_{Bi} and C_{Se} are the concentrations of Bi^{3+} and Se^{2-}, respectively.

$$\Delta G = RT \times \ln \frac{J_{sp}}{K_{sp}} \quad (1)$$

$$J_{sp} = C_{Bi}{}^2 \times C_{Se}{}^3 \quad (2)$$

The calculated formation energy of Bi_2Se_3 nanodots (ΔG) reaches the high value of 662.1 kJ mol^{-1}, indicating their very fast nucleation process and the formation of ultrasmall size.[31]

The small size of Bi_2Se_3 nanodots leads to their poorly resolved X-ray powder diffraction (XRD) pattern (Figure 1c), which only exhibits the main characteristic (015) and (01 11) peaks in comparison with that of pure Bi_2Se_3 synthesized without BSA and the standard hexagonal Bi_2Se_3 (JCPDS card no. 33-0214). The amorphous characteristic of BSA is also evident in the pattern. To identify the valence states of elements in the BSA-Bi_2Se_3 nanodots, X-ray photoelectron spectroscopy (XPS) was used to determine their binding energies (Figure 1d,e). The binding energies of Bi $4f_{5/2}$ are located at 163.4 eV, and that of Bi $4f_{7/2}$ are observed at 157.9 eV.[32−35] In addition, the binding energies of S $2p_{1/2}$ (164.8 eV) and S $2p_{3/2}$ (163.7 eV) are overlapped with that of Bi 4f and could be assigned to thiol groups from BSA. The single peak at 53.9 eV in Figure 1e is attributed to the binding energy of Se 3d from Se^{2-}, which demonstrates the absence of other selenium species and the purity of ultrasmall Bi_2Se_3 nanodots.

The surface BSA on the resultant Bi_2Se_3 nanodots ensures their excellent disperseability in different media, including deionized water (DI), 0.9% NaCl solution (NS), neutral phosphate buffer solution (PBS), and piperazineethanesulfonic acid (HEPES). A similar hydrodynamic size (~6 nm) is observed in these colloids, as determined by the dynamic light scattering (DLS) shown in Figure 1f. In contrast, a large hydrodynamic size (~400 nm) is observed for Bi_2Se_3 nanoparticles synthesized without BSA (Figure S1c). The surface BSA also makes these colloids extremely stable, as characterized by the similar size in different media measured after 1 week (Figure S1d).

The ultraviolet−visible (UV−vis) absorbance was measured for ultrasmall BSA-Bi_2Se_3 nanodots dispersed in deionized water with different concnetrations from 21 μg mL^{-1} to 655 μg mL^{-1} (Figure S2a). A broad absorbance in the NIR window is obtained in these solutions due to the intrinsic narrow gap of Bi_2Se_3, and an excellent linearity between the absorbance at 808 nm and the concentration of Bi_2Se_3 was observed (Figure S2b). According to the Lambert−Beer law ($A/L = \alpha C$, where A is the absorption intensity, L is the length of the cuvette, C is the concentration, and α is the extinction coefficient), the extinction coefficient (α) of ultrasmall BSA-Bi_2Se_3 nanodots at 808 nm was calculated to be 3.1 L g^{-1} cm^{-1}, which is comparable to that of widely used photothermal transducers such as graphene oxide[36] and gold nanostructures[18,37] for photothermal therapy.

The broad NIR absorbance and comparable extinction coefficient of BSA-Bi_2Se_3 nanodots suggest high photothermal conversion efficiency. Figure 2a presents photographs of aqueous solutions of different amounts of ultrasmall BSA-Bi_2Se_3 nanodots captured by an infrared camera, when they were irradiated by an 808 nm laser with a power density of 0.75 W cm^{-2} for 600 s. The solution temperature rose rapidly and strongly depended on the concentration of Bi_2Se_3 nanodots (Figure 2b), *e.g.*, the temperature of Bi_2Se_3 nanodots solution (655 μg mL^{-1}) dramatically increased from 25.5 to 67 °C after irradiation for 600 s. The result indicates their high photothermal conversion efficiency, which is calculated to be 50.7% (refer to Figure S3 and calculation details in the Supporting Information).[38,39] More importantly, ultrasmall BSA-Bi_2Se_3 nanodots exhibit excellent photostability, demonstrated by constant temperature profiles in 5 cycles of heating and cooling processes (Figure S3c).

DOI: 10.1021/acsnano.6b06067
ACS Nano 2016, 10, 11145−11155

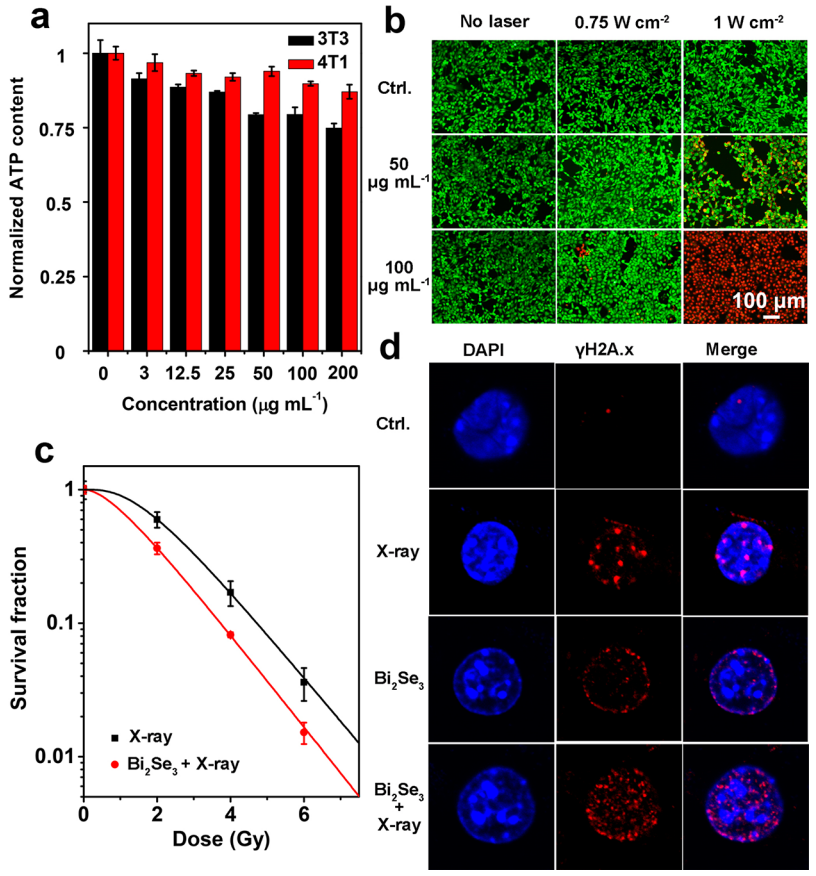

Figure 3. (a) Cell vialbilities of 3T3 and 4T1 cells determined by ATP assay, after they were cultured with different concentrations (0, 3, 12.5, 25, 50, 100, and 200 μg mL^{-1}) of BSA-Bi_2Se_3 nanodots for 24 h. (b) Live−dead staining images of 4T1 cells treated with BSA-Bi_2Se_3 nanodots solutions (0, 50, 100 μg mL^{-1}) and different densities of an 808 nm laser (0, 0.75, 1 W cm^{-2}), respectively. (c) Colony formation assay of 4T1 cells irradiated with X-rays at a dose of 0, 2, 4, 6, and 8 Gy in the presence or absence of BSA-Bi_2Se_3 nanodots (100 μg mL^{-1}). (d) DNA damage analysis of 4T1 cells treated with/without BSA-Bi_2Se_3 nanodots, X-ray exposure, or both. The concentration of BSA-Bi_2Se_3 nanodots was 100 μg mL^{-1}, and the dose of X-rays was 6 Gy.

The remarkable photothermal conversion efficiency and excellent stability of the BSA-Bi_2Se_3 nanodots highlight their great potential in PA imaging and photothermal cancer therapy. Figure 2c shows the *in vitro* dependence of PA imaging on the concentration of BSA-Bi_2Se_3 nanodots irradiated with a 680 nm laser. The PA signal linearly increases as the concentration of Bi_2Se_3 increases from 0 to 43, 85, 170, and 340 μg mL^{-1}. Prior to testing the feasibility of photothermal ablation of cancer cells, the cytotoxicity of BSA-Bi_2Se_3 nanodots toward healthy and cancer cells (3T3, mouse embryo fibroblasts cells, and 4T1, murine breast cancer cells) was investigated by both adenosine-triphosphate (ATP) assay and standard methyl thiazolyl tetrazolium (MTT) assay, respectively. The metabolic activity was evaluated by an ATP assay kit. As shown in Figure 3a, BSA-Bi_2Se_3 nanodots have a slight impact on the generation of ATP, even their concentration is up to 200 μg mL^{-1}, which demonstrates that BSA-Bi_2Se_3 nanodots have an excellent biocompatibility. Complementary MTT assay further confirms the low cytotoxicity of BSA-Bi_2Se_3 nanodots, *e.g.*, 70% and 75% of 3T3 and 4T1 cells were survived under 200 μg mL^{-1} of BSA-Bi_2Se_3 nanodots (Figure S4).

Based on these results, 4T1 cells were cultured with ultrasmall BSA-Bi_2Se_3 nanodots at concentration of 0, 50, and 100 μg mL^{-1} and then exposed to an 808 nm laser with a power density of 0, 0.75, and 1 W cm^{-2}, respectively. The live and dead cells were stained green and red, respectively (Figure 3b), which clearly show that the proportion of dead cells (red) increased with increasing laser power density and increasing content of BSA-Bi_2Se_3 nanodots. Cancer cells were completely killed with 100 μg mL^{-1} BSA-Bi_2Se_3 nanodots and 1 W cm^{-2} laser power density.

As mentioned previously, Bi_2Se_3 nanostructures also show great potential in CT imaging, and Figure S5 presents the variation in signal intensity of CT images from BSA-Bi_2Se_3 nanodots and commercial iopromide, respectively, as the molar concentration of Bi or I change from 0 to 0.6, 1.3, 2.5, and 5.0 mM. The X-ray absorption coefficient of BSA-Bi_2Se_3 nanodots is about 70.6 HU mM^{-1}, which is far greater than that of commercial iopromide (3.9 HU mM^{-1}). If the units of Bi_2Se_3 concentration are expressed by gram per liter (0 to 0.4, 0.8, 1.6, and 3.2 g L^{-1} for Bi_2Se_3 nanodots, respectively), the X-ray absorption coefficient is about 107.8 HU L g^{-1}, which is approximately 3.5 times higher than that of commercial iopromide (30.7 HU L g^{-1}).

The high X-ray absorption coefficient of Bi_2Se_3 nanodots is attributed to the fast attenuation of X-rays in Bi_2Se_3, which is the sum of attenuation of X-rays in Bi and Se. Their overall X-ray attenuation coefficient can be calculated by eq 3:

$$\mu_{Bi_2Se_3} = 0.64\mu_{Bi} + 0.36\mu_{Se} \quad (3)$$

DOI: 10.1021/acsnano.6b06067
ACS Nano 2016, 10, 11145−11155

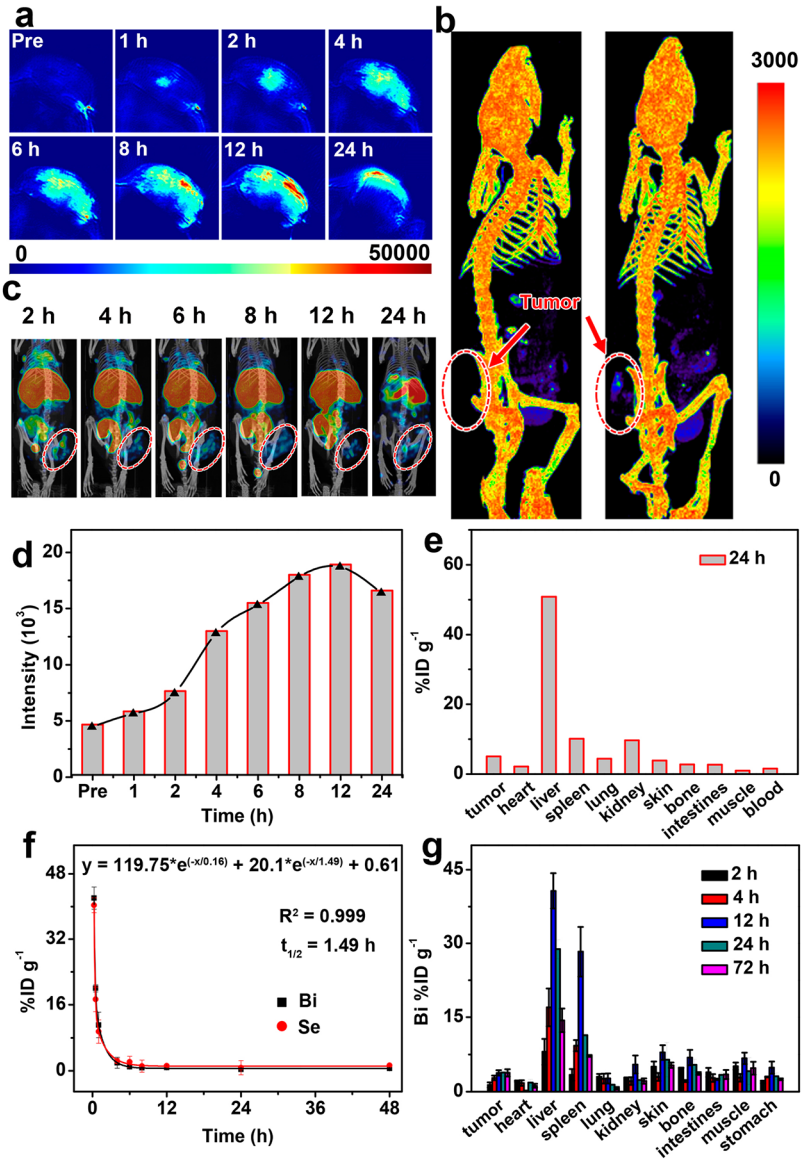

Figure 4. (a) *In-vivo* tumor PA-imaging performed at different times (preinjection and 1, 2, 4, 6, 8, 12, and 24 h post-injection) before and after intravenous injection of ultrasmall Bi_2Se_3 nanodots (7.3 mg kg^{-1}). (b) 3D CT images of tumor-bearing mice before (left) and after (right) injection of BSA-Bi_2Se_3 nanodots. (c) Time-dependent SPECT/CT images of the mice injected with ^{99m}Tc-labeled ultrasmall Bi_2Se_3 nanodots (tumors marked with red circles). (d) Time-dependent PA signal intensity of the tumor. (e) Distribution of BSA-Bi_2Se_3 nanodots by counting γ rays in the tissues and organs of a mouse sacrificed at 24 h postinjection. (f) Relative contents of Bi and Se in the blood collected at 0.25, 0.5, 1, 2, 4, 8, 12, 24, and 48 h post-intravenous injection (7.3 mg kg^{-1}). (g) Bi distribution in tissues at different time points of 2, 4, 12, 24, and 72 h post-injection of BSA-Bi_2Se_3 nanodots.

Where μ_{Bi} and μ_{Se} are the attenuation coefficients of Bi and Se, respectively. The effective atomic number of Bi_2Se_3 can be calculated by Equation 4:

$$\bar{Z} = \sqrt[2.94]{2 \times Z_{Bi}^{2.94} + 3 \times Z_{Se}^{2.94}} \quad (4)$$

where Z_{Bi} and Z_{Se} are the atomic numbers of Bi and Se, respectively.[40−42] The calculated effective atomic number is 109, much higher than that of individual elements.

The sensitivity of BSA-Bi_2Se_3 nanodots to X-rays also indicates their potential in radiotherapy, which can kill malignant cells by breaking the deoxyribonucleic acid (DNA) strands through ionizing radiation. A colony formation assay of 4T1 cells irradiated by X-rays with a dose of 0, 2, 4, 6, and 8 Gy in the presence or absence of BSA-Bi_2Se_3 nanodots (100 μg mL^{-1}) was performed (Figure 3c,d and Figure S6), and the results were fitted with a multitarget single-hitting model which can be expressed by eq 5:

$$S = 1 - [1 - \exp(-D/D_0)] \wedge N \quad (5)$$

where S is the cell survival fraction after exposure to X-rays, D is the X-ray dose, D_0 is the dose of X-rays when the survival fraction drops to 63% in the exponential curve, which means the average dose of X-rays for killing cells,[43] and N is an extrapolated value to characterize the cells' self-repairing capability against X-ray irradiation. A large value of N means a strong resistance to X-rays. In addition to these parameters, the quasi-threshold dose (D_q) and the sensitivity enhancement ratio (SER) could be calculated from eqs 6 and 7), and they are important indicators for evaluating the radiation efficiency.[44,45]

DOI: 10.1021/acsnano.6b06067
ACS Nano 2016, 10, 11145−11155

$$D_q = \ln(N \times D_0) \quad (6)$$

$$\mathrm{SER} = D_0(\mathrm{ctrl.})/D_0(\mathrm{exp.}) \quad (7)$$

As displayed in Figure 3c, the survival fraction dramatically dropped after irradiation with different doses of X-rays (0−8 Gy) in the presence of ultrasmall BSA-Bi_2Se_3 nanodots, in comparison with the cells irradiated only with the same dose of X-rays. In the presence of Bi_2Se_3 nanodots, N dropped from 3.66 to 2.00, which suggests deterioration of cell self-repairing capability after X-rays irradiation. In addition, D_0 is decreased from 1.33 to 1.25 Gy, and the quasi-threshold dose (D_q) is also reduced from 1.58 to 0.92 Gy, which allows higher accumulative damage to cells. The overall radio-enhancement ratio (*i.e.*, SER) is calculated to be 6%.

The enhanced sensitizing effects of Bi_2Se_3 nanodots can be further demonstrated by the γH2A.x analysis in Figure 3d, which characterizes the DNA damage of cells. The results demonstrate that DNA strands were seriously damaged after irradiation with 6 Gy X-rays in the presence of BSA-Bi_2Se_3 nanodots (100 μg mL^{-1}), in comparison with cells cultured with nanodots or only irradiated with X-rays.

To evaluate the *in vivo* PA imaging performance, mice bearing 4T1 tumors with a volume of 100 mm^3 were intravenously injected with 200 μL ultrasmall BSA-Bi_2Se_3 nanodots solution (7.8 mg kg^{-1} for the dose), and the PA images at different times post-injection are shown in Figure 4a. The tumor contrast was gradually enhanced with the time after injection and reached its maximum at 12 h post-injection, due to the accumulation of Bi_2Se_3 nanodots in the tumor. The contrast was slightly decreased 24 h post-injection. The signal intensity was further quantified in Figure 4d, which clearly shows the gradual increase to the maximum, followed by a decrease.

Figure 4b shows the CT images of mice bearing 4T1 tumors marked by red circles, after intratumoral injection of 50 μL Bi_2Se_3 nanodots solution (0.078 mg Bi_2Se_3). The CT value for the tumor region is significantly increased from 51 HU to 467 HU, owing to the large attenuation of X-rays by Bi_2Se_3 nanodots. One advantage of the ultrasmall BSA-Bi_2Se_3 nanodots is their surface multifunctional groups (−SH, −COOH, and $-NH_2$) in BSA, which can be chelated with radioactive ^{99m}Tc for SPECT imaging to detect tumors. The ^{99m}Tc-labeled BSA-Bi_2Se_3 nanodots were purified by ultrafiltration to remove the free ^{99m}Tc nuclide, and the radiolabeling yield is calculated to be 90.8% by determining the radioactivity of supernatant and filtrate. The labeled and unlabeled nanodots have a similar hydrodynamic size (Figure S7a), which demonstrate their excellent colloidal stability during labeling. The radiostability was determined by the relative radioactivity of ^{99m}Tc dissociated and nondissociated from labeled BSA-Bi_2Se_3 nanodots. Figure S7b demonstrates that ^{99m}Tc was tightly bound with BSA-Bi_2Se_3 nanodots, and the overall relative radioactivity was maintained around 90%. To confirm the coordination of ^{99m}Tc with functional groups (−SH, −COOH, and $-NH_2$) of BSA, pure BSA was also labeled with ^{99m}Tc and then purified by the same procedures (labeling yield is 99.5%). The radiostability of labeled BSA was assessed by the same method, and the result in Figure S7c shows that about 94.1% of radioactivity was maintained after stirred with FBS for 24 h. These results illustrate the high radiostability of labeled nanodots *in vitro*.

Figure 4c presents the SPECT/CT images of a tumor-bearing-mouse collected at different intervals after intravenous injection of ^{99m}Tc-labeled BSA-Bi_2Se_3 nanodots, in which the tumor lesions are clearly marked with red circles. The Bi_2Se_3 nanodots accumulated in the tumor could be estimated according to the SPECT/CT results collected at different time points after intravenous injection. The tumoral CT intensity increased from a prevalue of 50 HU to about 60 HU and up to 94 HU as the time was prolonged from 2 to 24 h after injection (Figure S8a), and the accumulated Bi_2Se_3 nanodots in tumor are calculated to be 1.9% ID g^{-1} (ID, injection dose). The normal tissue of the contralateral region has almost a constant CT value due to the absence of accumulated Bi_2Se_3 nanodots.

The accumulation of Bi_2Se_3 nanodots in the main organs can be also quantified by measuring the radioactivity of labeled nanodots. Figure S8b shows the accumulation of Bi_2Se_3 nanodots in the tumor from 2 to 24 h post-injection, which was quantified by the signal intensity within the selected area shown in Figure 4c, and the maximum accumulation is 2.2% ID g^{-1}, which is consistent with the CT result. Figure 4e shows the distribution of BSA-Bi_2Se_3 nanodots in tumor and other organs by counting their γ-ray emissions after the mouse was sacrificed at 24 h post-injection to harvest tumor and major organs. The dots distribution follows an order of liver > spleen ≈ kidney, and the stronger signals in liver (51% ID g^{-1}) and spleen (10% ID g^{-1}) are attributed to their rich phagocytes. The results show that about 10% ID g^{-1} of Bi_2Se_3 nanodots could be excreted through the kidney, which could reduce their potential side effects. The accumulation of nanodots in tumor increased to 5% ID g^{-1} at 24 h post-injection.

The circulation of ultrasmall BSA-Bi_2Se_3 nanodots in blood was examined by determining the contents of Bi and Se in blood samples collected at different time points after intravenous injection of nanodots. Figure 4f shows the time-dependent contents of Bi and Se in the blood determined by inductively coupled plasma-optical emission spectroscopy (ICP-OES). Similar circulation behavior of Bi and Se was observed, indicating the remarkable stability of the Bi_2Se_3 nanodots in the blood environment. The blood circulation half-life of Bi_2Se_3 was quantified to be 9.5 ± 1.9 h based on the exponent quadratic model.

To further demonstrate the metabolism of BSA-Bi_2Se_3 nanodots, the time-dependent biodistributions of Bi in main organs were determined and are shown in Figure 4g. Figure 4g illustrates the distribution of Bi in different organs harvested at 2, 4, 12, 24, and 72 h after the mice were sacrificed. As expected, Bi_2Se_3 nanodots are mainly distributed in reticuloendothelial organs such as the liver and spleen, which are the major biological barriers to translating administrated nanomaterials. The content of Bi in liver increased to 8.0% ID g^{-1} in the first 2 h, reached the maximum (40.7% ID g^{-1}) at 12 h post-injection, and then decreased to 14.4% ID g^{-1} at 72 h. The Bi content in spleen also reached its maximum (28.3% ID g^{-1}) at 12 h post-injection and was then reduced to 7.2% ID g^{-1} 72 h post-injection. The high uptake of nanodots in the liver is due to the significantly slower blood flow relative to the systemic circulation (~1000 folds slow), which leads to more nanomaterials interacting with Kupffer cells, B cells, and endothelial cells.[46] The lower uptake of nanodots in the spleen is attributed to the differences in cell phenotype.[46] Compared with the liver and spleen, the tumor, heart, lung, intestine, skin, bone, kidney, and muscle have lower Bi contents. The

DOI: 10.1021/acsnano.6b06067
ACS Nano 2016, 10, 11145−11155

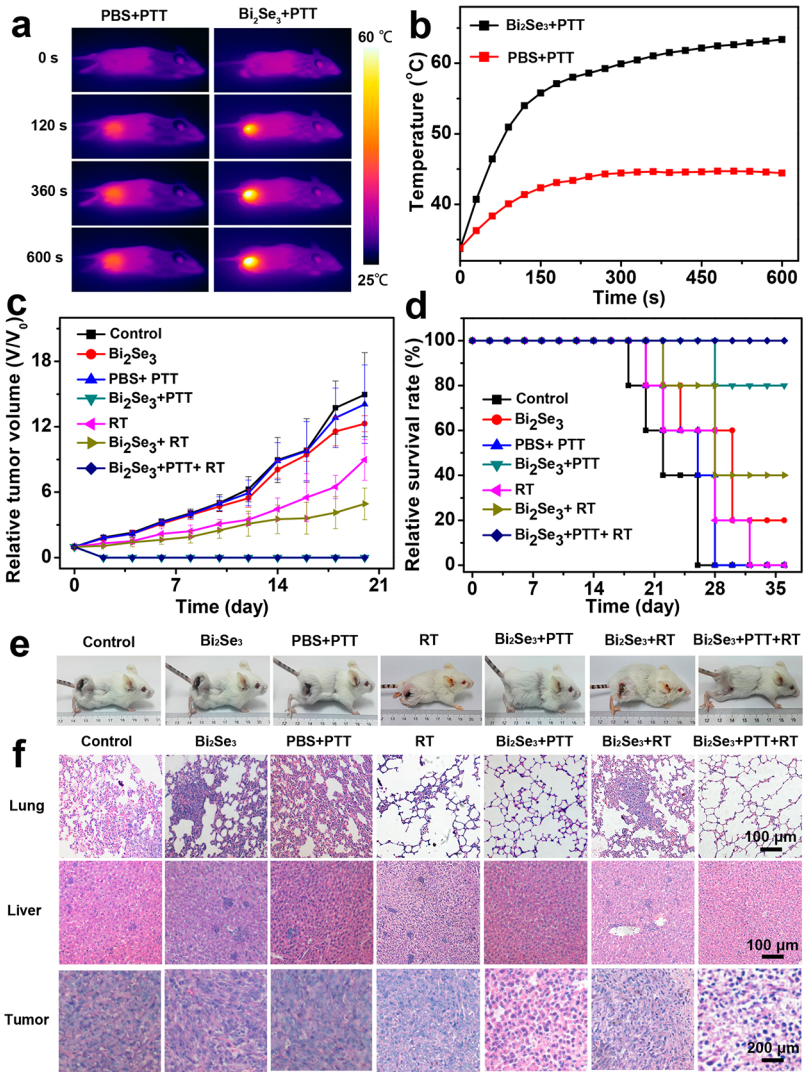

Figure 5. (a) Infrared thermal photographs of the tumor-bearing mice injected with PBS (left colcumn) and Bi_2Se_3 nanodots (right colcumn, dose = 7.3 mg kg^{-1}, irradiated 12 h post-injection), acquired at different times under NIR laser (808 nm) irradiation with a power density of 1 W cm^{-2}. (b) Temperature elevation of the tumor region with irradiation time. (c,d) Comparison of relative tumor volume and survival rate for each treatment group. (e) Photographs of representative mice for each treatment group to demonstrate the therapeutic efficacy. (f) Images of lung, liver, and tumor slices stained with hematoxylin and eosin for the different groups.

maximum accumulation of Bi in the tumor is about 4% ID g^{-1}, obtained at 12 h post-injection.

The above biodistribution results suggest that the treatment of cancer (*i.e.*, PTT and RT) should be carried out at 12 h after intravenous injection of BSA-Bi_2Se_3 nanodots. To test the feasibility of accumulated nanodots for combined photothermal therapy and X-ray radiotherapy of cancer through their outstanding performance of photothermal conversion and X-ray sensitization, seven groups of mice bearing tumors were selected to study the therapeutic efficacy, which are referred as (a) mice without any treatment (group 1, control); (b) mice injected with BSA-Bi_2Se_3 nanodots only (group 2, Bi_2Se_3); (c) mice irradiated with the NIR laser after injection of PBS (group 3, PBS + PTT); (d) mice irradiated with X-rays only (group 4, RT); (e) mice irradiated with the NIR laser after injection of BSA-Bi_2Se_3 nanodots (group 5, Bi_2Se_3 + PTT); (f) mice irradiated with X-rays after injection of BSA-Bi_2Se_3 nanodots (group 6, Bi_2Se_3 + RT); and (g) mice irradiated with the NIR laser and X-rays after injection of BSA-Bi_2Se_3 nanodots (group 7, Bi_2Se_3 + PTT + RT).

Figure 5a,b clearly demonstrates that the tumor temperature of the mouse injected with ultrasmall BSA-Bi_2Se_3 nanodots was elevated rapidly from 33.4 to 63.4 °C (ΔT = 30 °C) within 600 s under exposure to an 808 nm laser with a power density of 1 W cm^{-2}. In contrast, the increment of tumor temperature of the mouse injected with PBS is only 10 °C. The tumor volumes and the weights of the mice were monitored every other day. The weights of mice treated and untreated slightly fluctuated around 20 g (shown in Figure S9). There is no big difference in the tumor volume for the mice from the groups of control, Bi_2Se_3, and PBS + PTT (Figure 5c), but the tumors were ablated in the group of mice injected with BSA-Bi_2Se_3 nanodots followed by PTT treatment, which reveals the outstanding photothermal therapeutic efficacy of BSA-Bi_2Se_3 nanodots. Despite the remarkable effects of X-ray irradiation inhibiting the growth of tumors, it is unable to completely eliminate the tumors through radiotherapy. Only the tumors in the mice injected with ultrasmall BSA-Bi_2Se_3 nanodots and then irradiated with NIR laser and X-rays can be completely eliminated.

DOI: 10.1021/acsnano.6b06067
ACS Nano 2016, 10, 11145−11155

The relative survival rates in Figure 5d further demonstrate the distinct differences among these groups. The mice lived well after injection of BSA-Bi_2Se_3 nanodots and treatment with a combination of PTT and RT (group 7). The 100% survival rate demonstrates their excellent synergetic effects against cancer. In case of the mice treated either with PTT or RT after injection of BSA-Bi_2Se_3 nanodots, the survival rates were 80% (group 5) and 40% (group 6), respectively, which indicate the dominant role of PTT in the combined therapy. Only 20% of the mice injected with BSA-Bi_2Se_3 nanodots (group 2) survived, and no one survived among the mice without any treatment (group 1), or irradiated with X-rays only (group 3), or injected with PBS and then irradiated with NIR (group 4). These results again demonstrate the remarkable synergistic effects of photothermal therapy and radiotherapy. Representative photographs of mice from each group are shown in Figure 5e, and other photographs acquired at different times during treatment are presented in Figure S10.

To confirm the successful treatment of tumors without metastasis, the main organs (heart, liver, spleen, lung, and kidney) of the mice were harvested and sliced for staining with hematoxylin and eosin (Figure 5f and Figure S11). Except for the mice from group 5 (Bi_2Se_3 + PTT) and group 7 (Bi_2Se_3 + PTT + RT), a certain amount of tumor metastasis to the lung and liver can be found. The lung tissue has lost its normal reticular function in groups 1 (control) and 3 (PBS + PTT), and the metastatic lesion exhibits fuscous pieces in Figure 5f. The serious necrosis of tumor cells is observed in groups 5 (Bi_2Se_3 + PTT) and 7 (Bi_2Se_3 + PTT + RT) after treatment. In addition, no metastasis was observed in the heart, spleen, or kidney, as shown in Figure S11. These results further confirm the great feasibility of combined photothermal therapy and radiotherapy for ablation of tumors.

CONCLUSION

In summary, ultrasmall Bi_2Se_3 nanodots stabilized with BSA were synthesized successfully through a facile aqueous route under ambient conditions. The ultrasmall Bi_2Se_3 nanodots exhibit low cytotoxicity, good biocompatibility, and strong broad NIR absorbance, which endow them with excellent performance in photoacoustic imaging and photothermal therapy. These ultrasmall Bi_2Se_3 nanodots also exhibit huge potential in CT imaging and enhanced RT due to their large attenuation coefficient. In addition, they were also applied in SPECT/CT imaging after labeling with ^{99m}Tc. These ultrasmall Bi_2Se_3 nanodots integrated with multimodal imaging and combined therapies show great potential for accurate diagnosis and treatment of cancer.

EXPERIMENTAL SECTION

Synthesis of Bi_2Se_3 Nanodots. A facile one-pot reaction was adopted to synthesize ultrasmall BSA-Bi_2Se_3 nanodots under ambient conditions. In a typical synthesis, 0.3 mmol gray selenium powder was dissolved in a mixture of 220 μL mercaptoethanol and 660 μL ethylenediamine. The resultant solution was mixed with 150 mL BSA aqueous solution (10 mg mL^{-1}) under vigorous magnetic stirring in a 250 mL round-bottomed flask and marked as solution A. 0.2 mmol bismuth chloride was dissolved in 10 mL hydrochloric acid (1.2 M) and marked as solution B. Then solution B was quickly added into solution A, and the thus-formed black solution was stirred for 2 h. The final black solution was centrifuged with a speed of 10000 rpm for 15 min, and the colloidal supernatant was filtrated with a 100 kDa membrane and washed with Milli-Q water (18.2 MΩ cm) for several times to remove free BSA and other impurities. The supernatant was then further dialyzed with a universal dialysis tube (cutoff molecule weight is = 8000−14000 D) for 3 days. The resultant solution was lyophilized for further use and characterization.

Characterization. The morphology of the resultant BSA-Bi_2Se_3 nanodots was observed with a transmission electron microscope (FEI Tecnai G20) operating with an accelerating voltage of 200 kV. Their crystal structure was determined by X-ray powder diffraction (Shimadzu XRD-6000) equipped with Cu−Kα_1 radiation, (λ = 0.15406 nm). Their UV−vis-NIR absorption was measured on a PerkinElmer Lambda 750 UV−vis-NIR spectrophotometer. The hydrodynamic sizes of the nanodots were determined by a Zetasizer Nano ZS.

ATP Assay. After 1.5 × 10^5 mouse embryo fibroblasts cells (3T3) and murine breast cancer cells (4T1) were seeded in 6-well plates and cultured for 24 h, different concentrations (0, 3, 12.5, 25, 50, 100, and 200 μg mL^{-1}) of BSA-Bi_2Se_3 nanodots were added into cells and cultured for another 24 h. Cells were then lysed by adding 200 μL lysate and centrifuged at 12000 rpm for 5 min to collect the supernatants. 100 μL of working solution was then injected into 96-well plates and kept out of light for 5 min to consume the background. Subsequently, 20 μL lysed cells solution was added and mixed with the working solution to produce chemiluminescence, which was detected by a microplate reader (Biotek, US).

MTT Assay. 3T3 and 4T1 cells were cultured in the standard cell media at 37 °C in a 5% CO_2 atmosphere. 1 ×10^4 cells were seeded into 96 well plates and incubated with different concentrations (0, 3, 12.5, 25, 50, 100, and 200 μg mL^{-1}) of Bi_2Se_3 nanodots for 24 h. Relative cell viabilities were determined by the standard 3-(4,5-dimethylthiazol-2-yl)-2,5-diphenyltetrazolium bromide (MTT) assay.

Staining Live/Dead Cells. Culture media containing different concentrations (0, 50, 100 μg mL^{-1}) of Bi_2Se_3 nanodots were used for culturing 4T1 cells (3 × 10^5 each well) for 24 h. These cells were then irradiated with an 808 nm laser with different power densities (0, 0.75, and 1 W cm^{-2}) for 600 s. A live/dead staining kit was used to differentiate the living cells and dead cells on a fluorescence microscope (Leica).

Colony Formation. To investigate the radiation sensitivity of Bi_2Se_3 nanodots to X-rays, colony formation and γH2A.x assays were performed. 4T1 cells were seeded in 60 mm dishes and incubated for 24 h, then Bi_2Se_3 solution was added to the dishes, forming a Bi_2Se_3 concentration of 100 μg mL^{-1}. Cells were incubated for another 24 h before irradiated with a dose of 2, 4, 6, and 8 Gy X-rays, respectively. The colony formation was analyzed after incubation for 10 days by counting the cells stained with crystal violet.

DNA Injury Detection. After being seeded on the coverslips and treated with 100 μg mL^{-1} Bi_2Se_3 for 24 h, 4T1 cells were irradiated with 6 Gy X-rays at a dose rate of 1.01 Gy min^{-1}. Then, the cells were subjected to 4% paraformaldehyde fixation for 10 min and washed 3 times with phosphate buffered saline. Subsequently, the cells were immersed in iced Triton X-100 for 30 min to rupture the cell membrane and washed 3 times with PBS. After that, the cells were immersed in a blocking buffer (1% bovine serum albumin in tris-buffered saline solution) for 1 h at room temperature. They were then further incubated with antihistone γH2A.x mouse monoclonal antibodies (diluted 1:500 with PBS) at 4 °C in the dark for overnight. Then, the cells were incubated in sheep antimouse secondary antibody (diluted 1:2000 with PBS) for 2 h at room temperature. After that, the cells were exposed to 20 μL Hoechst stain, and the cell nuclei were dyed for 5 min before the cells were washed 5 times with PBS. Finally, the cells obtained were observed with a confocal microscope (PerkinElmer UltraViewVoX).

Photothermal Effect, Photostability, and Photothermal Conversion Efficiency. An 808 nm laser was used for estimating the photothermal performance of Bi_2Se_3 nanodots solutions with different concentrations (Bi_2Se_3: 0, 164, 327, 655 μg mL^{-1}). The power density was 0.75 W cm^{-2}, and the irradiation time was 600 s. The change of temperature was recorded with an infrared thermal imaging instrument (FLIR, A65). To evaluate the photostability, 5 cycles of alternating heating and cooling were carried out by turning

DOI: 10.1021/acsnano.6b06067
ACS Nano 2016, 10, 11145−11155

the laser on for 10 min and then turning off until the temperature decreased to room temperature.

To evaluate the photothermal conversion efficiency, a Bi_2Se_3 nanodots solution was heated to a steady temperature with an 808 nm laser at a power density of 0.75 W cm^{-2} and then naturally cooled to the ambient temperature. The photothermal conversion efficiency η was calculated as follows:

$$\eta = hS(T_{max} - T_{max,water})/I(1 - 10^{-A_{808}}) \quad (8)$$

$$hS = \sum mC_p/\tau_s \quad (9)$$

$$\tau_s = -t/\ln \theta \quad (10)$$

$$\theta = (T_{amb} - T)/(T_{amb} - T_{max}) \quad (11)$$

where h is the heat transfer coefficient, S is the surface area of container, and T_{max} and $T_{max,\ water}$ are the maximum steady temperatures for Bi_2Se_3 nanodots solution and water (56.6 and 26.5 °C, respectively), I is the incident laser power density (0.75 W cm^{-2}), and A_{808} is the absorbance of nanodots solution at 808 nm (A_{808} = 0.86). m is the mass (1.0 g) and C_p is the heat capacity [4.2 × 10^3 kJ (kg °C)$^{-1}$] of water. θ is the dimensionless driving force temperature, T_{amb} is the ambient temperature, and τ_s is the sample system time constant (τ_s = 386 s).

Multimodal Imaging Experiments. *Photoacoustic (PA) Imaging.* *In vitro* and *in vivo* PA imaging were performed on the multispectral optoacoustic tomography scanner (MSOT, iThera Medical). A series of Bi_2Se_3 nanodots solutions with concentrations of 0, 43, 85, 170, and 340 μg mL^{-1} were prepared for *in vitro* testing. To evaluate the imaging performance *in vivo*, a tumor-bearing nude mouse was anaesthetized and scanned with MSOT before and after intravenous injection of Bi_2Se_3 nanodots solution (655 μg mL^{-1}, 200 μL).

CT Imaging. *In vitro* and *in vivo* CT images were scanned in an accurate mode with 615 mA tube current and 55 kV tube voltage. To evaluated the *in vitro* CT imaging performance, Bi_2Se_3 nanodots solutions and the commercial iopromide were measured with the same concentrations (0, 0.6, 1.3, 2.5, and 5 mM for Bi/I ions) under the same conditions. For *in vivo* CT imaging, the 4T1 tumor-bearing mice were intratumorally and intravenously injected with BSA-Bi_2Se_3 nanodots, respectively.

SPECT-CT Imaging. Radioactive Technetium-99m (^{99m}Tc purchased from Shanghai GMS Pharmaceutical Co., Ltd.) was labeled onto BSA-Bi_2Se_3 nanodots. To label the nuclide, BSA-Bi_2Se_3 nanodots solution (1637.5 μg mL^{-1}, 500 μL) was mixed with fresh stannous chloride ($SnCl_2$, 5 mg mL^{-1} in 0.1 M HCl), and the nuclide (about 2 mCi) was added and stirred for 1 h at ambient temperature, then the solution was ultrafiltrated to remove the free ^{99m}Tc and concentrated to about 200 μL. The obtained ^{99m}Tc-BSA-Bi_2Se_3 nanodots were injected intravenously into tumor-bearing mice, and the SPECT-CT images were collected various times.

To test the labeling stability of ^{99m}Tc on Bi_2Se_3 nanodots *in vitro*, the labeled nanodots were purified by ultrafiltration (Ultrafree-PF filters, 100 kDa, Millipore) to remove the free ^{99m}Tc. The labeled nanoparticles were then diluted to 2 mL with 10% FBS and stirred for 2, 4, 6, 8, and 24 h, respectively. At each time point, 200 μL solution was taken and diluted with 10%FBS and then ultrafiltrated to remove the ^{99m}Tc dissociated from the labeled nanodots. The stability was calculated by the relative radioactivity of ^{99m}Tc dissociated and nondissociated from labeled BSA-Bi_2Se_3 nanodots. To confirm the coordination of ^{99m}Tc with functional groups (−SH, −COOH, and $-NH_2$) of BSA, pure BSA (37.5 mg mL^{-1}) was labeled with ^{99m}Tc by the same procedure. The stability of ^{99m}Tc labeled with BSA was also assessed by the same method.

Blood Circulation. Blood samples were collected from the retinal veins of heathy BALB/c mice before and after injection of Bi_2Se_3 nanodots solution (655 μg mL^{-1}, 200 μL). Five mice were used to collect their blood at the time of 0, 0.25, 0.5, 1, 2, 4, 8, 12, 24, 36, and 48 h post-injection, respectively. The collected blood samples were digested with the mixture of HNO_3/H_2O_2 (2:1 v/v) for quantification of Bi and Se by inductively coupled plasma-optical emission spectroscopy (ICP-OES). The time-dependent Bi/Se concentrations in blood were fitted with a two-compartmental model to determine the blood half-life.

Biodistribution. The time-dependent biodistribution of Bi_2Se_3 nanodots in major organs or tissues, such as tumor, heart, liver, spleen, lung, kidney, skin, bone, intestines, muscle, blood, and stomach was determined by ICP-OES. The organs or tissues were digested by the similar method applied to the blood samples. The data from each time point (2, 4, 12, 24, and 72 h) were represented by samples from four mice, respectively, injected with 200 μL Bi_2Se_3 nanodots solutions (655 μg mL^{-1}).

Therapy Effects of Bi_2Se_3 Nanodots. Photothermal therapy (PTT), radiotherapy (RT), and their combination were adopted to evaluate the therapeutic efficacy against cancer. An 808 nm laser (1 W cm^{-2} for 600 s) was used for PTT, and 6 Gy X-rays (rate of 1.01 Gy min^{-1}) were applied in RT. The injections are 200 μL of PBS or 200 μL of Bi_2Se_3 nanodots solution (655 μg mL^{-1}).

Seven groups (n = 5) of mice were referred as (a) mice without any treatment (group 1, Control); (b) mice injected with Bi_2Se_3 nanodots (group 2, Bi_2Se_3); (c) mice treated with the NIR laser after injection of PBS (group 3, PBS + PTT); (d) mice treated with X-rays irradiation after injection of PBS (group 4, RT); (e) mice treated with the NIR laser after injection of Bi_2Se_3 nanodots (group 5, Bi_2Se_3 + PTT); (f) mice treated with X-rays after injection of Bi_2Se_3 nanodots (group 6, Bi_2Se_3 + RT); and (g) mice sequentially treated with the NIR laser and X-rays after injection of Bi_2Se_3 nanodots (group 7, Bi_2Se_3 + PTT + RT). During the treatment, the weights of mice and the volumes of tumor were monitored. The tumor volume V (mm^3) was calculated by the formula $V = a \times b^2/2$, in which a and b were the length and width of the tumor, respectively. The relative survival rate was calculated after the whole treatment (36 days).

Histology Analysis. The major organs (lung, liver, heart, spleen, and kidney) were harvested from mice in each group, then dipped into formalin, and embedded in paraffin. Slices with a thickness of 5 μm were incised and stained with hematoxylin and eosin (H&E). The cell states of the tumors or organs were observed with a microscope.

ASSOCIATED CONTENT

Supporting Information

The Supporting Information is available free of charge on the ACS Publications website at DOI: 10.1021/acsnano.6b06067.

Additional characterization and results (PDF)

AUTHOR INFORMATION

Corresponding Authors

*E-mail: nanoelechem@hnu.edu.cn.

*E-mail: zhenli@suda.edu.cn.

ORCID

Zhen Li: 0000-0003-0333-7699

Notes

The authors declare no competing financial interest.

ACKNOWLEDGMENTS

Z.L. acknowledges support from the National Natural Science Foundation of China (81471657, 81527901), the 1000 Plan for Young Talents, and Jiangsu Specially Appointed Professorship. The authors also are grateful for support from the Jiangsu Provincial Key Laboratory of Radiation Medicine and Protection and the Priority Academic Development Program of Jiangsu Higher Education Institutions (PAPD) and for the discussion with Dr. Tania Silver.

DOI: 10.1021/acsnano.6b06067
ACS Nano 2016, 10, 11145−11155

REFERENCES

(1) Cheng, L.; Wang, C.; Feng, L. Z.; Yang, K.; Liu, Z. Functional Nanomaterials for Phototherapies of Cancer. *Chem. Rev.* **2014**, *114*, 10869−10939.

(2) Barreto, J. A.; O'Malley, W.; Kubeil, M.; Graham, B.; Stephan, H.; Spiccia, L. Nanomaterials: Applications in Cancer Imaging and Therapy. *Adv. Mater.* **2011**, *23*, H18−H40.

(3) Jakhmola, A.; Anton, N.; Vandamme, T. F. Inorganic Nanoparticles based Contrast Agents for X-ray Computed Tomography. *Adv. Healthcare Mater.* **2012**, *1*, 413−431.

(4) Na, H. B.; Song, I. C.; Hyeon, T. Inorganic Nanoparticles for MRI Contrast Agents. *Adv. Mater.* **2009**, *21*, 2133−2148.

(5) Lin, J.; Wang, M.; Hu, H.; Yang, X. Y.; Wen, B.; Wang, Z. T.; Jacobson, O.; Song, J. B.; Zhang, G. F.; Niu, G. Multimodal-Imaging-Guided Cancer Phototherapy by Versatile Biomimetic Theranostics with UV and γ-Irradiation Protection. *Adv. Mater.* **2016**, *28*, 3273−3279.

(6) Momeni, A.; Rahimian, G.; Kiasi, A.; Amiri, M.; Kheiri, S. Effect of Licorice *versus* Bismuth on Eradication of Helicobacter Pylori in Patients with Peptic Ulcer Disease. *Pharmacogn. Res.* **2014**, *6*, 341−344.

(7) Delchier, J. C.; Malfertheiner, P.; Thieroff-Ekerdt, R. Use of a Combination Formulation of Bismuth, Metronidazole and Tetracycline with Omeprazole as a Rescue Therapy for Eradication of Helicobacter Pylori. *Aliment. Pharmacol. Ther.* **2014**, *40*, 171−177.

(8) Zhou, L. Y.; Zhang, J. Z.; Song, Z. Q.; He, L. H.; Li, Y. Q.; Qian, J. M.; Bai, P.; Xue, Y.; Wang, Y.; Lin, S. R. Tailored *versus* Triple Plus Bismuth or Concomitant Therapy as Initial Helicobacter Pylori Treatment: a Randomized Trial. *Helicobacter* **2016**, *21*, 91−95.

(9) Graham, D. Y. Helicobacter Pylori Update: Gastric Cancer, Reliable Therapy, and Possible Benefits. *Gastroenterology* **2015**, *148*, 719−731.

(10) Wei, B. X.; Zhang, X. J.; Zhang, C.; Jiang, Y.; Fu, Y. Y.; Yu, C. S.; Sun, S. K.; Yan, X. P. Facile Synthesis of Uniform-Sized Bismuth Nanoparticles for CT Visualization of Gastrointestinal Tract. *ACS Appl. Mater. Interfaces* **2016**, *8*, 12720−12726.

(11) Poffo, C. M.; de Lima, J. C.; Souza, S. M.; Trichês, D. M.; Nogueira, T. P. O.; Borges, Z. V.; Manzato, L. Structural, Optical and Photoacoustic Study of Milled and Melted Bi_2Se_3. *J. Mol. Struct.* **2014**, *1076*, 737−742.

(12) Liu, J.; Zheng, X. P.; Yan, L.; Zhou, L. J.; Tian, G.; Yin, W. Y.; Wang, L. M.; Liu, Y.; Hu, Z. B.; Gu, Z. J.; et al. Bismuth Sulfide Nanorods as a Precision Nanomedicine for *in Vivo* Multimodal Imaging-Guided Photothermal Therapy of Tumor. *ACS Nano* **2015**, *9*, 696−707.

(13) Preihs, C.; Arambula, J. F.; Lynch, V. M.; Siddik, Z. H.; Sessler, J. L. Bismuth- and Lead-Texaphyrin Complexes: towards Potential α-core Emitters for Radiotherapy. *Chem. Commun.* **2010**, *46*, 7900−7902.

(14) Ma, M.; Huang, Y.; Chen, H. R.; Jia, X. Q.; Wang, S. G.; Wang, Z. Z.; Shi, J. L. Bi_2S_3-embedded Mesoporous Silica Nanoparticles for Efficient Drug Delivery and Interstitial Radiotherapy Sensitization. *Biomaterials* **2015**, *37*, 447−455.

(15) Wang, Y.; Wu, Y. Y.; Liu, Y. J.; Shen, J.; Lv, L.; Li, L. B.; Yang, L. C.; Zeng, J. F.; Wang, Y. Y.; Zhang, L. W.; et al. BSA-Mediated Synthesis of Bismuth Sulfide Nanotheranostic Agents for Tumor Multimodal Imaging and Thermoradiotherapy. *Adv. Funct. Mater.* **2016**, *26*, 5335−5344.

(16) Wang, S. G.; Li, X.; Chen, Y.; Cai, X. J.; Yao, H. L.; Gao, W.; Zheng, Y. Y.; An, X.; Shi, J. L.; Chen, H. R. A Facile One-Pot Synthesis of a Two-Dimensional MoS_2/Bi_2S_3 Composite Theranostic Nanosystem for Multi-Modality Tumor Imaging and Therapy. *Adv. Mater.* **2015**, *27*, 2775−2782.

(17) Li, J.; Jiang, F.; Yang, B.; Song, X. R.; Liu, Y.; Yang, H. H.; Cao, D. R.; Shi, W. R.; Chen, G. N. Topological Insulator Bismuth Selenide as a Theranostic Platform for Simultaneous Cancer Imaging and Therapy. *Sci. Rep.* **2013**, *3*, 1998.

(18) Xie, H. H.; Li, Z. B.; Sun, Z. B.; Shao, J. D.; Yu, X. F.; Guo, Z. N.; Wang, J. H.; Xiao, Q. L.; Wang, H. H.; Wang, Q. Q.; et al. Metabolizable Ultrathin Bi_2Se_3 Nanosheets in Imaging-Guided Photothermal Therapy. *Small* **2016**, *12*, 4136−4145.

(19) Song, G. S.; Liang, C.; Gong, H.; Li, M. F.; Zheng, X. C.; Cheng, L.; Yang, K.; Jiang, X. Q.; Liu, Z. Core−Shell MnSe@Bi_2Se_3 Fabricated *via* a Cation Exchange Method as Novel Nanotheranostics for Multimodal Imaging and Synergistic Thermoradiotherapy. *Adv. Mater.* **2015**, *27*, 6110−6117.

(20) Cheng, L.; Shen, S. D.; Shi, S. X.; Yi, Y.; Wang, X. Y.; Song, G. S.; Yang, K.; Liu, G.; Barnhart, T. E.; Cai, W. B.; et al. $FeSe_2$-Decorated Bi_2Se_3 Nanosheets Fabricated *via* Cation Exchange for Chelator-Free ^{64}Cu-Labeling and Multimodal Image-Guided Photothermal-Radiation Therapy. *Adv. Funct. Mater.* **2016**, *26*, 2185−2197.

(21) Song, G. S.; Liang, C.; Yi, X.; Zhao, Q.; Cheng, L.; Yang, K.; Liu, Z. Perfluorocarbon-Loaded Hollow Bi_2Se_3 Nanoparticles for Timely Supply of Oxygen under Near-Infrared Light to Enhance the Radiotherapy of Cancer. *Adv. Mater.* **2016**, *28*, 2716−2723.

(22) Cheng, Y. L.; Li, F. H.; Mladenov, E.; Iliakis, G. The Yield of DNA Double Strand Breaks Determined after Exclusion of Those Forming from Heat-Labile Lesions Predicts Tumor Cell Radiosensitivity to Killing. *Radiother. Oncol.* **2015**, *116*, 366−373.

(23) Cai, X. L.; Wang, C.; Yu, W. Q.; Fan, W. J.; Wang, S.; Shen, N.; Wu, P. C.; Li, X. Y.; Wang, F. D. Selenium Exposure and Cancer Risk: an Updated Meta-Analysis and Meta-Regression. *Sci. Rep.* **2016**, *6*, 19213.

(24) Zhang, X. D.; Yang, J.; Song, S. S.; Long, W.; Chen, J.; Shen, X.; Wang, H.; Sun, Y. M.; Liu, P. X.; Fan, S. J. Passing Through the Renal Clearance Barrier: Toward Ultrasmall Sizes with Stable Ligands for Potential Clinical Applications. *Int. J. Nanomed.* **2014**, *9*, 2069−2072.

(25) Yu, M. X.; Zheng, J. Clearance Pathways and Tumor Targeting of Imaging Nanoparticles. *ACS Nano* **2015**, *9*, 6655−6674.

(26) Chen, X. Q.; Li, Z.; Bai, Y.; Sun, Q.; Wang, L. Z.; Dou, S. X. Room-Temperature Synthesis of $Cu_{2-x}E$ (E = S, Se) Nanotubes with Hierarchical Architecture as High-Performance Counter Electrodes of Quantum-Dot-Sensitized Solar Cells. *Chem. - Eur. J.* **2015**, *21*, 1055−1063.

(27) Chen, X. Q.; Li, Z.; Dou, S. X. Ambient Facile Synthesis of Gram-Scale Copper Selenide Nanostructures from Commercial Copper and Selenium Powder. *ACS Appl. Mater. Interfaces* **2015**, *7*, 13295−13302.

(28) Han, C.; Sun, Q.; Cheng, Z. X.; Wang, J. L.; Li, Z.; Lu, G. Q.; Dou, S. X. Ambient Scalable Synthesis of Surfactant-Free Thermoelectric CuAgSe Nanoparticles with Reversible Metallic-n-p Conductivity Transition. *J. Am. Chem. Soc.* **2014**, *136*, 17626−17633.

(29) Chen, X. Q.; Bai, Y.; Li, Z.; Wang, L. Z.; Dou, S. X. Ambient Synthesis of One-/Two-Dimensional CuAgSe Ternary Nanotubes as Counter Electrodes of Quantum-Dot-Sensitized Solar Cells. *ChemPlusChem* **2016**, *81*, 414−420.

(30) Mao, F. X.; Guo, J.; Zhang, S. H.; Yang, F.; Sun, Q.; Ma, J. M.; Li, Z. Solvothermal Synthesis and Electrochemical Properties of S-doped Bi_2Se_3 Hierarchical Microstructure Assembled by Stacked Nanosheets. *RSC Adv.* **2016**, *6*, 38228−38232.

(31) Han, C.; Li, Z.; Lu, G. Q.; Dou, S. X. Robust Scalable Synthesis of Surfactant-Free Thermoelectric Metal Chalcogenide Nanostructures. *Nano Energy* **2015**, *15*, 193−204.

(32) Han, C.; Yang, J.; Yan, C.; Li, Y.; Liu, F. Y.; Jiang, L. X.; Ye, J. C.; Liu, Y. X. The Electrochemical Self-Assembly of Hierarchical Dendritic Bi_2Se_3 Nanostructures. *CrystEngComm* **2014**, *16*, 2823−2834.

(33) Yeh, Y. C.; Ho, P. H.; Wen, C. Y.; Shu, G. J.; Sankar, R.; Chou, F. C.; Chen, C. W. Growth of the Bi_2Se_3 Surface Oxide for Metal−Semiconductor−Metal Device Applications. *J. Phys. Chem. C* **2016**, *120*, 3314−3318.

(34) Tsipas, P.; Xenogiannopoulou, E.; Kassavetis, S.; Tsoutsou, D.; Golias, E.; Bazioti, C.; Dimitrakopulos, G. P.; Komninou, P.; Liang, H.; Caymax, M.; et al. Observation of Surface Dirac Cone in High-Quality Ultrathin Epitaxial Bi_2Se_3 Topological Insulator on AlN(0001) Dielectric. *ACS Nano* **2014**, *8*, 6614−6619.

(35) Desai, N. D.; Ghanwat, V. B.; Khot, K. V.; Mali, S. S.; Hong, C. K.; Bhosale, P. N. Effect of Substrate on the Nanostructured Bi_2Se_3

DOI: 10.1021/acsnano.6b06067
ACS Nano 2016, 10, 11145−11155

Thin Films for Solar Cell Applications. *J. Mater. Sci.: Mater. Electron.* **2016**, *27*, 2385−2393.
(36) Robinson, J. T.; Tabakman, S. M.; Liang, Y. Y.; Wang, H. L.; Sanchez Casalongue, H.; Vinh, D.; Dai, H. J. Ultrasmall Reduced Graphene Oxide with High Near-infrared Absorbance for Photothermal Therapy. *J. Am. Chem. Soc.* **2011**, *133*, 6825−6831.
(37) Yang, X.; Yang, M. X.; Pang, B.; Vara, M.; Xia, Y. N. Gold Nanomaterials at Work in Biomedicine. *Chem. Rev.* **2015**, *115*, 10410−10488.
(38) Zeng, J. F.; Cheng, M.; Wang, Y.; Wen, L.; Chen, L.; Li, Z.; Wu, Y. Y.; Gao, M. Y.; Chai, Z. F. Photothermal Therapy: pH-Responsive Fe(III)−Gallic Acid Nanoparticles for *In Vivo* Photoacoustic-Imaging-Guided Photothermal Therapy. *Adv. Healthcare Mater.* **2016**, *5*, 745−745.
(39) Sun, C. X.; Wen, L.; Zeng, J. F.; Wang, Y.; Sun, Q.; Deng, L. J.; Zhao, C. J.; Li, Z. One-Pot Solventless Preparation of PEGylated Black Phosphorus Nanoparticles for Photoacoustic Imaging and Photothermal Therapy of Cancer. *Biomaterials* **2016**, *91*, 81−89.
(40) Seltzer, S. M. Calculation of Photon Mass Energy-Transfer and Mass Energy-Absorption Coefficients. *Radiat. Res.* **1993**, *136*, 147−170.
(41) Lee, N.; Choi, S. H.; Hyeon, T. Nano-Sized CT Contrast Agents. *Adv. Mater.* **2013**, *25*, 2641−2660.
(42) Zhang, S. H.; Sun, C. X.; Zeng, J. F.; Sun, Q.; Wang, G. L.; Wang, Y.; Wu, Y.; Dou, S. X.; Gao, M. Y.; Li, Z. Ambient Aqueous Synthesis of Ultrasmall PEGylated $Cu_{2-x}Se$ Nanoparticles as a Multifunctional Theranostic Agent for Multimodal Imaging Guided Photothermal Therapy of Cancer. *Adv. Mater.* **2016**, *28*, 8927−8936.
(43) Park, C.; Papiez, L.; Zhang, S. C.; Story, M.; Timmerman, R. D. Universal Survival Curve and Single Fraction Equivalent Dose: Useful Tools in Understanding Potency of Ablative Radiotherapy. *Int. J. Radiat. Oncol., Biol., Phys.* **2008**, *70*, 847−852.
(44) Rofstad, E. K. Retention of Cellular Radiation Sensitivity in Cell and Xenograft Lines Established from Human Melanoma Surgical Specimens. *Cancer Res.* **1992**, *52*, 1764−1769.
(45) Li, M. F.; Zhao, Q.; Yi, X.; Zhong, X. Y.; Song, G. S.; Chai, Z. F.; Liu, Z.; Yang, K. Au@MnS@ZnS Core/Shell/Shell Nanoparticles for Magnetic Resonance Imaging and Enhanced Cancer Radiation Therapy. *ACS Appl. Mater. Interfaces* **2016**, *8*, 9557−9564.
(46) Tsoi, K. M.; MacParland, S. A.; Ma, X. Z.; Spetzler, V. N.; Echeverri, J.; Ouyang, B.; Fadel, S. M.; Sykes, E. A.; Goldaracena, N.; Kaths, J. M.; et al. Mechanism of Hard-Nanomaterial Clearance by the Liver. *Nat. Mater.* **2016**, *15*, 1212−1221.

DOI: 10.1021/acsnano.6b06067
ACS Nano 2016, 10, 11145−11155